# Effects of cryogenic temperature on tensile and impact properties in a medium-entropy VCoNi alloy

Yang, Dae Cheol; Jo, Yong Hee; Ikeda, Yuji; Körmann, Fritz; Sohn, Seok Su

**DOI**
10.1016/j.jmst.2021.02.034

**Publication date**
2021

**Document Version**
Final published version

**Published in**
Journal of Materials Science and Technology

Journal of Materials Science & Technology 90 (2021) 159–167

Contents lists available at ScienceDirect

Journal of Materials Science & Technology

journal homepage: www.elsevier.com/locate/jmst

Research Article

# Effects of cryogenic temperature on tensile and impact properties in a medium-entropy VCoNi alloy

Dae Cheol Yang[a], Yong Hee Jo[b], Yuji Ikeda[c], Fritz Körmann[d,e], Seok Su Sohn[a,*]

[a] Department of Materials Science and Engineering, Korea University, 02841 Seoul, South Korea
[b] Metallic Materials Division, Korea Institute of Materials Science, 51508 Changwon, South Korea
[c] Institute for Materials Science, University of Stuttgart, Pfaffenwaldring 55, 70569 Stuttgart, Germany
[d] Max-Planck-Institut für Eisenforschung, Max-Planck-Straβe 1, 40237 Düsseldorf, Germany
[e] Department of Materials Science and Engineering, Delft University of Technology, Mekelweg 2, 2628 CD Delft, The Netherlands

ARTICLE INFO

*Article history:*
Received 16 December 2020
Revised 23 January 2021
Accepted 3 February 2021
Available online 28 April 2021

*Keywords:*
Medium-entropy alloy
Cryogenic temperature
Tensile property
Charpy impact property
Stacking fault energy

ABSTRACT

Multi-principal element alloys usually exhibit outstanding strength and toughness at cryogenic temperatures, especially in CrMnFeCoNi and CrCoNi alloys. These remarkable cryogenic properties are attributed to the occurrence of deformation twins, and it is envisaged that a reduced stacking fault energy (SFE) transforms the deformation mechanisms into advantageous properties at cryogenic temperatures. A recently reported high-strength VCoNi alloy is expected to exhibit further notable cryogenic properties. However, no attempt has been made to investigate the cryogenic properties in detail as well as the underlying deformation mechanisms. Here, the effects of cryogenic temperature on the tensile and impact properties are investigated, and the underlying mechanisms determining those properties are revealed in terms of the temperature dependence of the yield strength and deformation mechanism. Both the strength and ductility were enhanced at 77 K compared to 298 K, while the Charpy impact toughness gradually decreased with temperature. The planar dislocation glides remained unchanged at 77 K in contrast to the CrMnFeCoNi and CrCoNi alloys resulting in a relatively constant and slightly increasing SFE as the temperature decreased, which is confirmed via *ab initio* simulations. However, the deformation localization near the grain boundaries at 298 K changed into a homogeneous distribution throughout the whole grains at 77 K, leading to a highly sustained strain hardening rate. The reduced impact toughness is directly related to the decreased plastic zone size, which is due to the reduced dislocation width and significant temperature dependence of the yield strength.



## 1. Introduction

Multi-principal element alloys (MPEAs), also referred to as high- or medium-entropy alloys (HEAs/MEAs), have been in the spotlight in structural applications because of their outstanding mechanical properties [1–4]. Notably, MPEAs have high configurational entropy compared to existing dilute alloys, which enables them to form a single face-centered cubic (fcc) solid-solution phase in a moderate range of the enthalpy of mixing or atomic size differences. Recently, among fcc-structured MPEAs, an equiatomic VCoNi alloy has been attracting considerable attention because of its yield strength of approximately 1 GPa and good ductility of 38%, which exceeds conventional dilute and concentrated solid-solution alloys [5]. The superior mechanical properties of the VCoNi alloy ensue from severe lattice distortion and slip-band refinement during deformation. Although lattice distortion is a common but unique property toward determining the strength of MPEAs, additional chemical strengthening has also been reported for these alloys. The V element has a larger misfit volume than other alloy elements, which consequently results in further lattice distortion and strength, as demonstrated via *ab initio* calculations and solute strengthening theories [6]. Furthermore, the VCoNi alloy is known to possess functional properties, such as superplasticity [7], as well as high resistance to corrosion and hydrogen embrittlement [8]. These remarkable mechanical and functional properties facilitate the application of these alloys to sustainable infrastructures and devices.

Additionally, MPEAs usually exhibit outstanding strength and toughness at cryogenic temperatures [9–11], especially for the two prototypical and well-studied alloys: (1) CrMnFeCoNi HEA, which exhibits an evident fracture toughness of ~260 kJ $m^{-2}$ that is relatively constant in a temperature range of 77–293 K [12]; they

* Corresponding author.
*E-mail address:* sssohn@korea.ac.kr (S.S. Sohn).

https://doi.org/10.1016/j.jmst.2021.02.034
1005-0302/

are comparable to the cryogenic steels used in industries, such as austenitic stainless steels and high-Ni steels, and (2) CrCoNi, which has superior mechanical properties when compared to CrMnFeCoNi alloys at 77 K and exhibits a Charpy V-notch impact toughness value as high as 340 J, even at a liquid helium temperature of 4 K [12,13]. The remarkable cryogenic properties of these two alloys are attributed to the occurrence of deformation twins. The critical twinning stress of CrCoNi is attained earlier than that of CrMnFeCoNi, thereby leading to better properties in the former. In addition to these alloys, dual-phase $Fe_{50}Co_{30}Cr_{10}V_{10}$ HEAs have been reported to exhibit a tensile strength of approximately 2 GPa and ductility of ~39% at 77 K through the deformation-induced phase transformation from fcc to body-centered cubic (bcc) and the significant strain partitioning effects between the parent and product phases [14]. The assumed underlying mechanism for the excellent cryogenic properties for the above-mentioned alloys is that the stacking fault energy (SFE) reduces with temperature, and hence, it converts deformation mechanisms to advantageous properties at cryogenic temperatures.

A primary deformation mechanism at ambient temperature for the VCoNi alloy is the dislocation-mediated plasticity, i.e., planar dislocation glide, which usually occurs for fcc-structured alloys with high SFEs. However, investigations into the variations in this mechanism at cryogenic temperatures remain unprecedented. Therefore, in this study, we aim to investigate the cryogenic tensile and impact properties of the VCoNi alloy and to reveal the underlying deformation mechanism with respect to SFE variations. We found through density-functional theory (DFT) calculations that the unusual temperature dependence of the SFE for VCoNi alloys is less sensitive to temperature variations and slightly increases as the temperature decreases, in contrast to the aforementioned alloys. Both the strength and ductility were improved at cryogenic temperatures, while the Charpy impact energy curves had similar behaviors to those of bcc alloys, contrary to existing fcc-structured MPEAs, although a ductile-to-brittle transition was absent. We elucidated this unusual behavior in terms of the temperature dependence of the yield strength and deformation mechanism.

## 2. Experimental and computational details

### 2.1. Fabrication

The master VCoNi alloy (150 g) was produced through a vacuum induction melting process (model: MC100V, Indutherm, Walzbachtal–Wossingen, Germany). The master alloys were prepared from commercially pure elements (V 99.95%; Co 99.95%; Ni 99.99%). The raw elements were stacked in a zirconia crucible together and then cast in a graphite mold to make ingots (length × width × thickness: 70 mm × 35 mm × 8 mm). The graphite mold was preheated to 100 °C for 0.5 h to remove the water vapor before placing it into a furnace. Before melting, the furnace chamber was evacuated to $6 \times 10^{-2}$ Pa and backfilled with high-purity argon gas to reach 0.06 MPa. This cleaning produce was repeated 10 times. The cast ingots were homogenized at 1473 K for 24 h in evacuated quartz ampules, water-quenched, and cold-rolled with a thickness reduction of 80%. For the homogenized blocks, an energy dispersive spectroscopy (EDS) reveals that the matrix composition is almost identical to the target composition (V 32.9 ± 0.4 at.%; Co 33.4 ± 0.5 at.%; Ni 33.7 ± 0.3 at.%), and secondary particles are mostly rich in V and O (V 35.1 ± 1.0 at.%; Co 17.1 ± 0.8 at.%; Ni 20.1 ± 1.4 at.%; O 27.7 ± 2.1 at.%). The 1.5 mm thick cold-rolled sheets were then annealed at 1173 K for 10 min and 1 h, and at 1223 K and 1273 K for 1 h in an Ar atmosphere, followed by water quenching.

For the Charpy impact test, the master VCoNi alloy (500 g) was prepared through a vacuum induction melting process (model: VTC 200V, Indutherm, Walzbachtal–Wossingen, Germany). Thereafter, the cast blocks (50 mm × 40 mm × 25 mm) were cold-rolled to a thickness of 11 mm through an identical thermomechanical treatment to the specimens used for the tensile tests. The cold-rolled sheets were then annealed at 1173 K for 1 h in an Ar atmosphere, followed by water quenching.

### 2.2. Microstructural characterization

The grain size and morphology of the fcc phase were investigated via electron backscatter diffraction (EBSD) and electron channeling contrast imaging (ECCI) analyses. The final mechanical polishing was conducted using a colloidal silica suspension for 1 h for removing damaged layers. The EBSD analysis was performed via field emission scanning electron microscopy (FE-SEM, JEOL, JSM-6500F, USA). The kernel average misorientation (KAM) approach was conducted for calculating the average misorientation of a given point relative to its neighbors. The KAM was calculated up to the first neighbor shell with a maximum misorientation angle of 5°. The KAM values reveal deformation-induced local orientation gradients. Local misorientation is induced by both the lattice rotation associated with geometrically necessary dislocations (GNDs) and the elastic strain field [15]. The GND accommodates the strains that can induce a non-uniform plastic deformation, which subsequently causes lattice curvature [16]. Because the influence of the elastic strain field is less than that of lattice rotation, local misorientation can be considerably related to GND [17]. Therefore, the GND map can be estimated directly through the KAM map using Eq. (1) [18]:

$$\rho_{GND}\left(m^{-2}\right) = \frac{2\theta}{ub} \tag{1}$$

where $\theta$ is the radian of the KAM value, $u$ is the unit length, and $b$ is the magnitude of the Burgers vector in the alloy. After substituting the KAM value calculated from the EBSD data into Eq. (1), the calculated dislocation density is used to draw the GND map in the orientation imaging microscopy analysis. Additionally, ECCI analyses were carried out using a Zeiss Merlin instrument (Zeiss Crossbeam 1540 EsB, Zeiss, Oberkochen, Germany).

### 2.3. Tensile and Charpy impact tests

Dog bone-shaped specimens were prepared by electrical discharge machining. The gauge length, width, and thickness of the tensile specimens were 25 mm, 5 mm, and 1.2 mm, respectively. Uniaxial tensile tests were carried out at room temperature (298 K) and cryogenic temperature (77 K) using a universal testing machine (model: 8801, Instron, Canton, MA, USA) at a crosshead speed of $25 \times 10^{-3}$ mm $s^{-1}$. The representative data were obtained by averaging three values at each datum point. Additionally, uniaxial tensile tests were also conducted at 773 K to investigate the temperature dependence of the yield strength for the alloy annealed at 1223 K for 1 h. The gauge length was marked by a Vickers microhardness tester (300 g load) to measure the strain using an optical microscope.

Charpy impact tests were performed on V-notch specimens (size: 55 mm × 10 mm × 10 mm, longitudinal–transverse (L–T) direction) in the range of 77–298 K using a Tinius Olsen impact tester with a 500 J capacity (model: FAHC-J-500-01, JT Toshi, Tokyo, Japan). After the impact tests were performed, fracture surfaces were observed using SEM. The tensile and Charpy impact tests were conducted three times for each datum point.

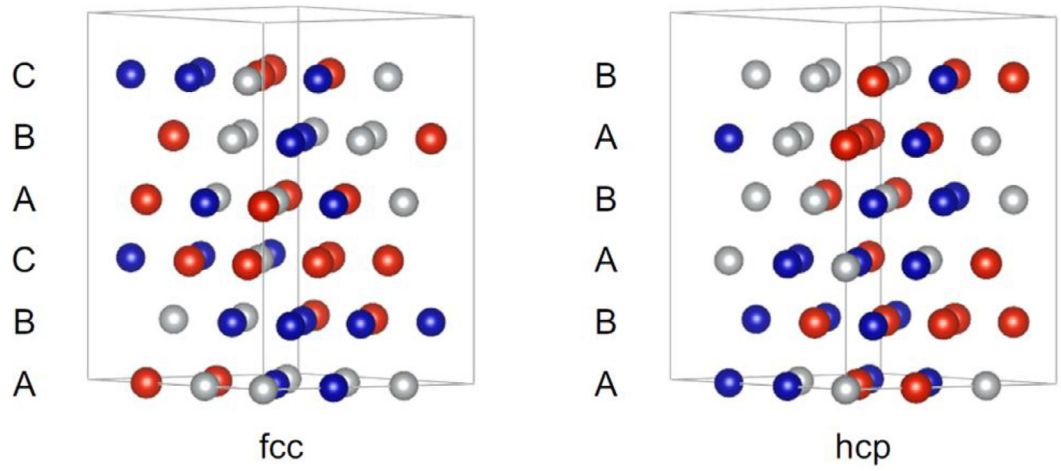


**Fig. 1.** Simulation cells with 54 atoms used in the present study. Spheres with different colors correspond to different elements. Among the ten investigated special quasi-random structure (SQS) configurations for each phase, one configuration is shown.

### 2.4. Ab initio calculations

The SFEs of VCoNi and CrCoNi in the fcc phase were computed based on the first-order axial Ising model (AIM1) [19] as

$$\mathrm{SFE} \approx \frac{2\left(F^{\mathrm{hcp}} - F^{\mathrm{fcc}}\right)}{A} \quad (2)$$

where $F^{\mathrm{hcp}}$ and $F^{\mathrm{fcc}}$ denote the Helmholtz free energy per atom of hcp and fcc, and $A$ denotes the area of the close-packed layer per atom.

To improve the computational accuracy, both the fcc and hexagonal close-packed (hcp) phases were modeled by 54-atom supercells with identical supercell shapes, as shown in Fig. 1. The fcc unit cell is represented along the <111> direction as the third axis and displays the "ABCABC" stacking of the close-packed {111} layers, while the hcp unit cell has the "ABABAB" stacking of the close-packed {0001} layers. These supercells have six layers, and each layer consists of nine atoms. Chemical disorder was simulated by a special quasi-random structure (SQS) [20] with minimization of the correlation functions of the first several nearest-neighbor pairs.

The *ab initio* calculations were performed within the DFT framework employing the Vienna Ab initio Simulation Package (VASP) code [21–23] and the projector-augmented wave method [24]. The exchange-correlation energy has been treated within the generalized gradient approximation (GGA) of the Perdew–Burke–Ernzerhof (PBE) form [25]. A plane wave cutoff energy of 300 eV was chosen for all calculations. The 3*d*4*s* orbitals of V, Cr, Co, and Ni were treated as the valence states. The Brillouin zones were sampled by a Γ-centered 6 × 6 × 4 *k*-point mesh for the 54-atom supercell models and by the Methfessel–Paxton scheme [26] with a smearing width of 0.1 eV. The total energies were minimized until they converged within $1 \times 10^{-3}$ eV per simulation cell. All the calculations were performed considering spin polarization. All magnetic moments on Cr were initially set to be antiparallel to those on Co and Ni-based on the results previously established using the coherent-potential approximation (CPA) [27]. The magnetic moments can adapt to an energetically more preferable orientation during the energetic minimization.

The equilibrium properties at 0 K were obtained by computing the total energies for six volumes approximately close to the equilibrium volume and then by fitting the obtained energy–volume functions to the Vinet equation of state [28,29]. To achieve better statistics, we considered ten inequivalent SQS models for each composition and each volume. The internal atomic coordinates were optimized until all the forces on the atoms converged within $5 \times 10^{-2}$ eV Å$^{-1}$. Table 1 summarizes the equilibrium properties obtained. The contribution of lattice vibrations to the Helmholtz energy at finite temperatures was derived from the obtained equilibrium properties at 0 K based on the Debye–Grüneisen model [27,30]. The SFE at finite temperatures was computed at the computational equilibrium volume of the fcc phase at the corresponding temperature.

**Table 1**
Computed equilibrium volumes and energies of VCoNi and CrCoNi at 0 K obtained by fitting to the Vinet equation of state. The energies are referenced to that of the fcc phase (shown in parentheses).

| | Volume (Å$^3$/atom) | | Energy (meV/atom) | |
|---|---|---|---|---|
| | fcc | hcp | fcc | hcp |
| CrCoNi | 10.92 | 10.91 | (0) | −7 |
| VCoNi | 11.41 | 11.41 | (0) | +6 |

## 3. Results

### 3.1. Microstructure of annealed VCoNi alloy

Fig. 2(a–d) shows the EBSD inverse pole figure (IPF) maps for the VCoNi alloy cold-rolled and recrystallized under four different annealing conditions. It is known that VCoNi consists of a single fcc solid solution at temperatures above 1173 K [5]. All the annealing conditions resulted in fully recrystallized structures, whose average grain sizes decreased from approximately 26 $\mu$m, 10 $\mu$m, and 5 $\mu$m to 3 $\mu$m as the annealing time and temperature decreased, as indicated by the $D_{\mathrm{fcc}}$. For convenience, the specimens are hereafter referred to as D26, D10, D5, and D3, respectively, according to their average grain size.

### 3.2. Room- and cryogenic-temperature mechanical properties

Fig. 3(a) shows the engineering stress–strain curves for the annealed VCoNi alloy deformed at 77 K and 298 K. The curves are expressed for two selective annealing conditions, while all the mechanical properties are listed in Table 2. The D5 specimen exhibited yield and tensile strengths of 710 MPa and 1172 MPa, respectively, at 298 K. As the testing temperature decreased, both the strength and ductility increased, resulting in 960 MPa and 1551 MPa for the yield and tensile strengths, respectively, and 56.7% ductility. For the fine-grained D3 specimen, the room-temperature

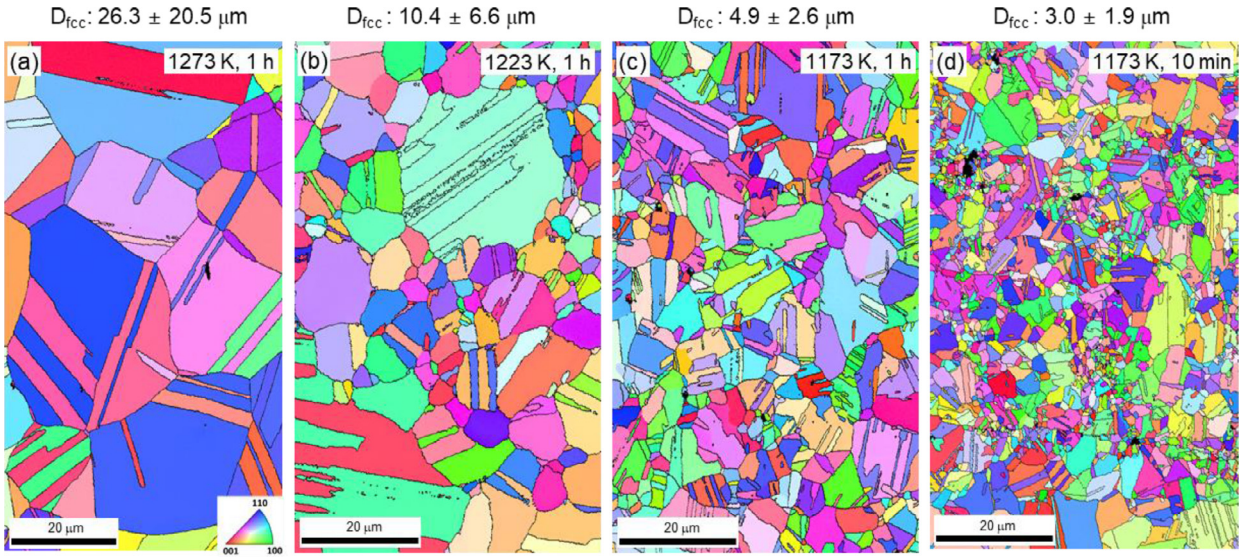


**Fig. 2.** Electron backscatter diffraction (EBSD) inverse pole figure (IPF) maps of the VCoNi alloy annealed at (a) 1273 K for 1 h, (b) 1223 K for 1 h, (c) 1173 K for 1 h, and (d) 1173 K for 10 min.

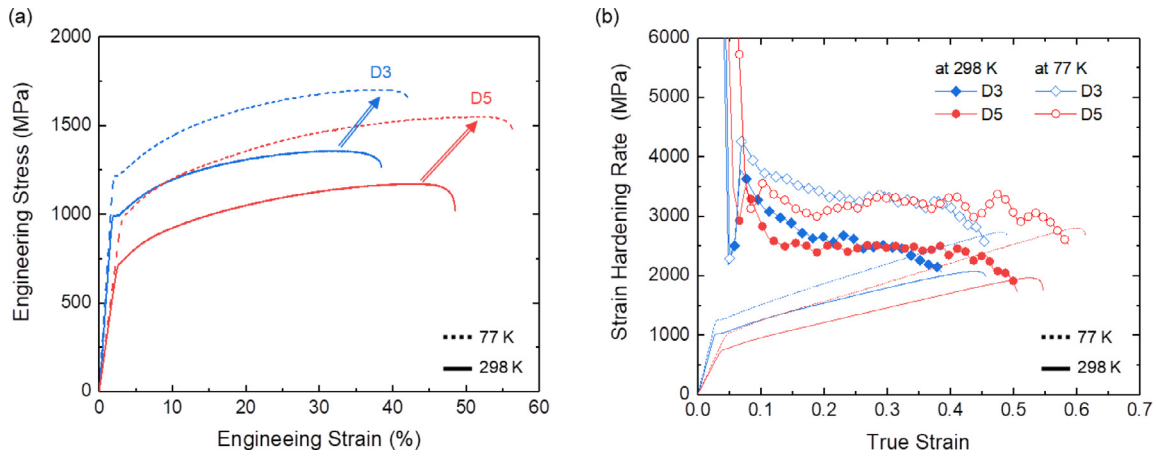


**Fig. 3.** Tensile properties at room- and cryogenic-temperatures for the annealed VCoNi alloy: (a) Engineering stress–strain curves, (b) Strain-hardening rate curves.

**Table 2**
Tensile properties at room and cryogenic temperatures for the VCoNi alloy annealed under the given conditions.

| Temperature | Specimen | Yield strength (MPa) | Tensile strength (MPa) | Elongation (%) |
|---|---|---|---|---|
| 298 K | D3 | 988 ± 31 | 1357 ± 24 | 38.4 ± 4.4 |
| | D5 | 710 ± 22 | 1172 ± 18 | 48.7 ± 3.8 |
| | D10 | 627 ± 17 | 1140 ± 11 | 52.0 ± 4.8 |
| | D26 | 501 ± 16 | 973 ± 7 | 70.0 ± 5.9 |
| 77 K | D3 | 1217 ± 30 | 1703 ± 24 | 42.1 ± 2.4 |
| | D5 | 960 ± 14 | 1551 ± 11 | 56.7 ± 3.4 |
| | D10 | 895 ± 19 | 1474 ± 8 | 58.7 ± 4.1 |
| | D26 | 710 ± 8 | 1271 ± 5 | 75.3 ± 5.5 |

yield strength of 988 MPa was similar to the cryogenic yield strength of D5. This alloy also exhibited enhanced strength and ductility at 77 K; thus, the tensile strength reached 1703 MPa with 42.1% ductility. The other specimens listed in Table 2 displayed an identical tendency for variations in mechanical properties when the testing temperature decreased.

Fig. 3(b) shows the true stress–strain and strain hardening rate curves of D3 and D5. The hardening rate gradually decreased for D3 at both 298 K and 77 K, while the rate was higher at 77 K. On the other hand, the rate curve at 298 K for D5 showed a plateau for strain values between 0.1 and 0.4. For the curve at 77 K, the rate increased from a strain value of 0.2, presenting a well-sustained high strain hardening rate. These persistent high rates delay the onset of plastic instability and lead to enhanced strength and ductility at 77 K.

### *3.3. Microstructural evolution with tensile deformation at room- and cryogenic- temperatures*

To investigate the deformation mechanism and associated transitions by testing the temperature of the VCoNi alloy, interrupted tensile tests were carried out for D5 at 298 K and 77 K with sequential plastic strain amounts of 0.05, 0.1, 0.2, and 0.4.

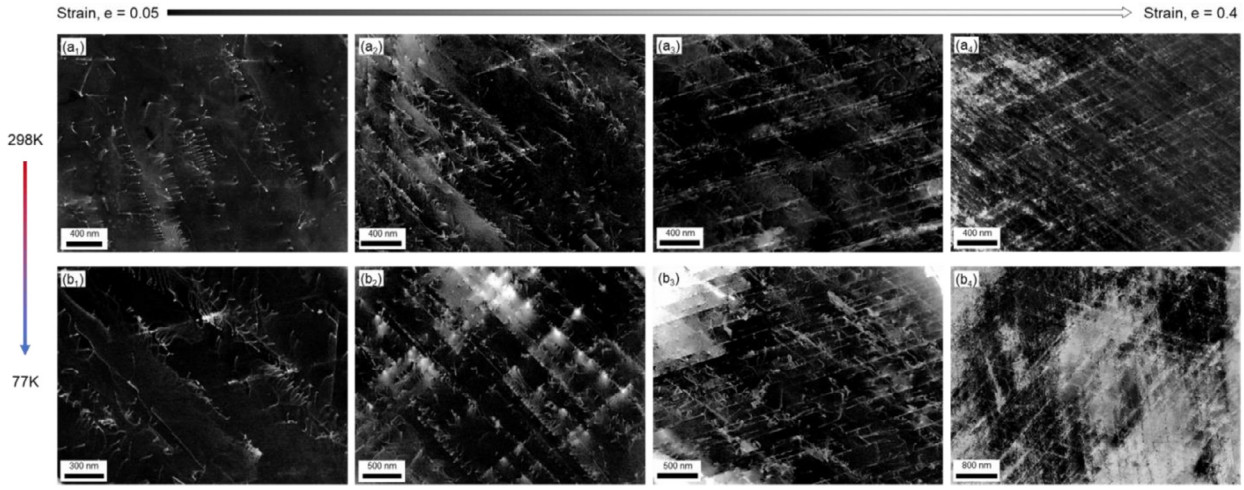


**Fig. 4.** ECCI micrographs of the tensile-deformed microstructures for the VCoNi alloy annealed at 1173 K for 1 h at sequential plastic strains: ($a_1$) $e$=0.05, ($a_2$) $e$=0.1, ($a_3$) $e$=0.2, and ($a_4$) $e$=0.4 at 298 K; ($b_1$) $e$=0.05, ($b_2$) $e$=0.1, ($b_3$) $e$=0.2, and ($b_4$) $e$=0.4 at 77 K.

Fig. 4($a_1$–$a_4$) displays the ECCI micrographs for the D5 specimens tested at 298 K. At a strain value of 0.05, individual dislocations were evidently identified and arranged in a row along the trace of the {111} plane, defined as the typical characteristic of planar glide initiation. At a strain value of 0.1, the slip traces were found along two independent {111} planes, and they started to form intertwined dislocation networks of planar dislocation arrays. With further deformation to 0.2 strain, the spacing of the slip band reduced to 81.1 nm, which refined the nano-sized dislocation substructures. As the applied strain increased up to 0.4, the average spacing between planar slip bands was further refined to 56.1 nm and the slip bands intersected more frequently. This nano-sized dislocation substructure effectively reduced the mean free path of dislocation glides owing to the high dislocation density in each intense slip band. This non-cell-forming structure strongly verified the difficulty of cross-slip [31,32], referred to as the Taylor lattice-like structure [33], which contributes to the high strain-hardening capability (Fig. 3). This pronounced slip planarity is attributed to high friction stresses caused by severe lattice distortion. It is difficult to overcome the stress required for gliding in this alloy through dislocation alone. Therefore, a collective gliding of dislocations on the same slip plane is necessary to overcome the stress, which leads to slip planarity [34].

The deformation structures at 77 K (Fig. 4($b_1$–$b_4$)) reveal that the VCoNi alloy behaves almost identical at 77 K and 298 K, even though the testing temperature decreased considerably. The individual dislocations are arrayed in rows, followed by planar glide, intersection of slip bands, and refinement of the slip band to successively form Taylor lattices at 298 K. The average slip band spacing decreased as the deformation progressed further, indicating 444 nm, 87.7 nm, and 60.4 nm at strains of 0.1, 0.2, and 0.4, respectively. These quantities are similar to those of the structures at 298 K, which also causes a reduction in the mean free path of the dislocation glides.

### 3.4. Charpy impact properties

The impact energy at 298 K was 183 J and gradually decreased to 125 J as the test temperature decreased to 77 K (Fig. 5). The observation of fracture surfaces in the inset of Fig. 5 reveals that a ductile-dimpled fracture prevails at 298 K and is maintained even at 77 K. It is particularly noteworthy that the appearance of the ductile fracture remains at cryogenic temperature, but the impact energy decreases, such as bcc alloys showing a ductile-to-brittle transition. This behavior is different from the temperature dependence of the impact or fracture toughness of previously reported fcc-based HEAs or MEAs, such as CrMnFeCoNi [10,35], CrCoNi [36], CrFeCoNi [37], and VCrFeCoNi [38,39]. The toughness of these alloys remains or even increases as the testing temperature decreases, which is known to be due to the transition of the deformation mechanism from slip to deformation twinning, the increased nano-twinning activity [10,35–37], or the formation of deformation-induced martensite [38] during plastic deformation. The present VCoNi alloy, in contrast, deformed by the planar glide of dislocations and subsequent formation of dislocation substructure, and not by transformation-induced plasticity (TRIP) or twinning-induced plasticity (TWIP). The underlying mechanism for this unfamiliar phenomenon will be clarified in the following sections.

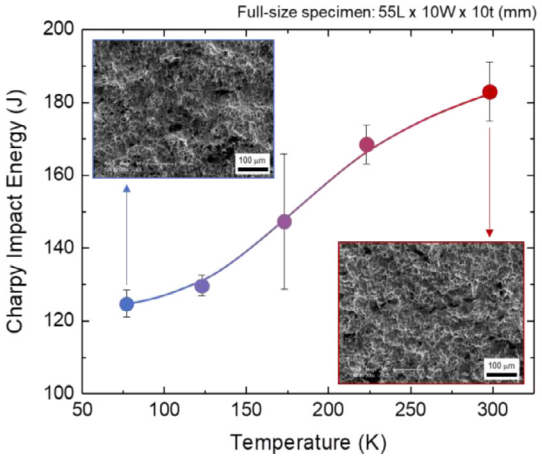


**Fig. 5.** Charpy impact energy as a function of test temperature for the VCoNi annealed at 1173 K for 1 h. SEM fractographs of the Charpy impact specimen fractured at 77 K and 298 K, showing a ductile fracture.

## 4. Discussion

### 4.1. Temperature dependence of deformation behavior

The mechanical properties of CrMnFeCoNi and CrCoNi, which are representative fcc HEAs/MEAs, are improved at cryogenic tem-

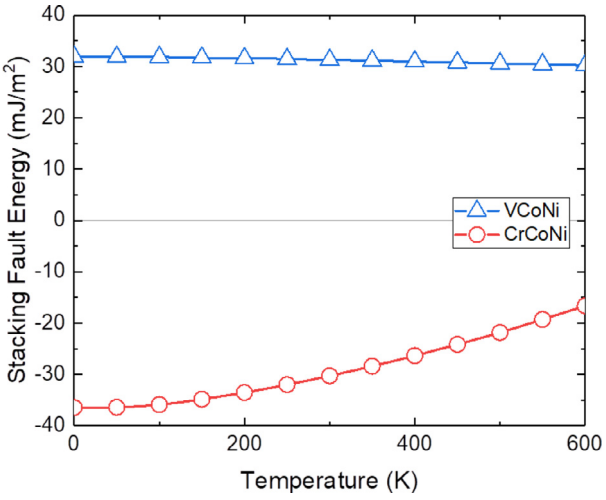


**Fig. 6.** Computed SFEs based on *ab initio* simulations as a function of temperature for VCoNi and CrCoNi alloys.

peratures because of the more active formation of deformation nano-twins, called the TWIP effect [12,40]. The variation in the deformation behaviors of such fcc alloys is generally interpreted by their SFEs, which reduce as temperature decreases [9,41–43]. The enhancement of mechanical properties at 77 K was also established for the VCoNi alloy, but a noteworthy difference was the unaffected deformation behaviors and remnant dislocation-mediated plasticity. According to the ECCI results, planar slip initially occurs and thereafter develops into the Taylor lattice with high-density dislocation walls (HDDWs) at both 298 K and 77 K. This result implies that the effect of temperature on the SFE of VCoNi would be insignificant or at least qualitatively different from those reported for, e.g., CrMnFeCoNi and CrCoNi. This motivates us to reveal the underlying mechanism in terms of the SFE.

To verify this expectation, we computed the SFE of VCoNi based on *ab initio* simulations, as represented in Fig. 6. For comparison, the SFE of CrCoNi is also shown. A negative SFE was found for CrCoNi at 0 K, which is consistent with previous *ab initio* results [44–47] and indicates that at 0 K the hcp phase is thermodynamically more stable than the fcc phase. A previous *ab initio* study indicated that chemical short-range order can increase the SFE of CrCoNi [46]. For CrCoNi, we found that the computed SFE decreased with decreasing temperature, consistent with our above-mentioned expectation. This trend is also consistent with a previous *ab initio* study (cf. Fig. 4 in Ref. [45]). Conversely, for VCoNi, the SFE was found to be relatively independent of temperature. A near-constant SFE for VCoNi was found, revealing that the deformation behavior of VCoNi remained rather unaffected by temperature as compared to the CrCoNi alloy. Note that these quantities do not necessarily reflect absolute SFEs, but capture the qualitative change in SFEs from their zero temperature values. For example, the experimental SFE of CrCoNi was determined to be 22 mJ m$^{-2}$ at 298 K by measuring the separation distance between Shockley partials [12], which could be partially attributed to short-range order not accounted for in the present simulations.

Various previous *ab initio* studies have shown that the temperature dependence of SFEs can vary qualitatively depending on the alloy or material system considered. For pure Al, Cu, and Ni, for example, finite-temperature calculations revealed a decrease in SFE with increasing temperature [48]. This is qualitatively different from that of, for example, FeMn alloys [49] or various other 3*d*-transition element multicomponent alloys, including the prototypical CrCoNi and CrMnFeCoNi, wherein SFEs are found to increase with temperature [45]. These examples underline how strongly SFEs can vary depending on temperature and composition, which is consistent with the qualitatively different trends found in the present work for VCoNi and CrCoNi.

The aforementioned remarkable properties at cryogenic temperatures of CrMnFeCoNi and CrCoNi alloys, specifically the enhancement of both strength and ductility from those at room temperature, have been explained by the TWIP or TRIP effect. The computed SFEs, however, imply that for VCoNi both the mechanisms are either not activated or less active at room temperature. Therefore, the enhanced strength and ductility of VCoNi must be attributed to other mechanisms. To reveal them, we focused on the dislocation density and distribution of localized deformation structures. Fig. 7($a_1$, $b_1$) shows the EBSD KAM maps of D10, which was 35% deformed at 298 K and 77 K. The misorientation is known to be caused by elastic distortions of the lattice resulting from arrays of GNDs [50]. It is evident that the KAM value was higher for the deformation at 77 K. The average KAM values were 0.79 and 1.14 at 298 K and 77 K, respectively. These values correspond to the GND density of 1.15 and 2.19 $\times$ 10$^{15}$ m$^{-2}$, confirming that the GND density is higher for the deformation at 77 K. At cryogenic temperatures, dislocations can readily accumulate owing to the suppression of dynamic recovery [51]. Lower dynamic recovery at 77 K would lead to a higher dislocation density, and therefore to higher strain hardening rates and a lower decrease in the strain hardening rate during deformation (Fig. 3(b)) [52].

An additional feature found in KAM maps is the distribution of misorientation. At 298 K, the grain boundaries were usually of a highly misoriented region, while both grain boundaries and lattices exhibited high KAM values at 77 K. This result indicates a tendency to form a relatively homogeneous network of dislocations at lower temperatures. The degree of deformation, however, varies with grain size, Schmid factor, and orientation; thus, an additional EBSD line profile analysis was conducted under regulated variables between the deformation conditions. Two lines were taken along directions $L_1$ and $L_2$, both being approximately parallel to the tensile direction of each specimen. Fig. 7($a_2$, $b_2$) confirms that the Schmid factor displays similar color levels for the grains of interest, and the average values along the line profiles are determined to be 0.313 (298 K) and 0.317 (77 K). A similar level of the Schmid factor excludes the effect of priority for slip systems to be activated during deformation. In addition, in Fig. 7($a_3$, $b_3$), the pole of the two grains is analogous to the [101] direction. However, the lattice rotation obtained along with the line profile supersedes the direction. Although the total misorientation at the end near the grain boundary is approximately identical to ~6° according to the point-to-origin misorientation plot, the profile at 77 K shows larger fluctuations and accumulated misorientations in lattices. Moreover, the GND density presented in Fig. 7($a_4$, $b_4$) reveals that it is higher at the grain boundaries for both temperatures, while it fluctuates more in lattices with higher values at 77 K.

Accordingly, the effects of deformation structures on the increase in both strength and ductility at 77 K are attributed to twofold contributions. Firstly, although the transition to TWIP or TRIP is absent in VCoNi alloys, the dislocation density increases under planar-slip dislocation-mediated plasticity. At both temperatures, dislocations are stored within the grain interior rather than freely gliding toward the grain boundaries because of the slip-band refinement [34]. A high density of slip bands with dense-packed dislocations (Fig. 4) proves that dislocations are stored in lattices while constructing HDDWs and fine dislocation structures. The measured spacing of slip bands is similar for both conditions, which is consistent with our DFT results for the SFEs, but the microscopic structure observation demonstrates the high dislocation density at 77 K and consequently the enhanced stress and strain-hardening rate according to Taylor's hardening. The slip band at 77 K can be regarded to contain a higher density of dislocations.

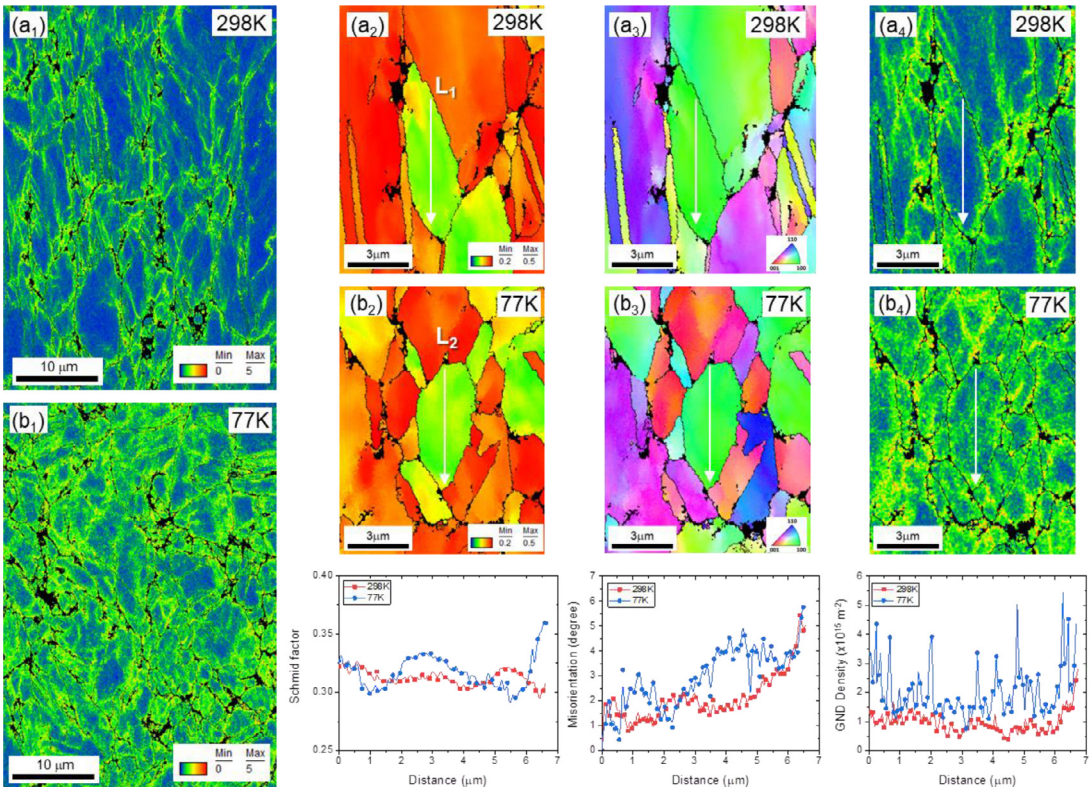


**Fig. 7.** EBSD KAM maps for D10, 35% deformation at ($a_1$) 298 K and ($b_1$) 77 K. Selective areas identifying the distribution of deformation structure by ($a_2$–$a_4$) IPF, Schmid factor, GND maps in ($a_1$), and ($b_2$–$b_4$) IPF, Schmid factor, GND maps in ($b_1$). Line profile data on $L_1$ (298 K) and $L_2$ (77 K) for each map are shown below.

Secondly, the well-sustained high strain-hardening rate results from the homogenous distribution of deformation structures. The Taylor lattice in the VCoNi alloy induces homogenous distributions of deformation with the aid of the mutual screening effect of planar slip bands having alternating signs that lower the stored energy [53]. Because of the lower temperature, the lower mobility and higher resistance to dislocation glide can restrict the further localization of the slip. This enables multiple glides and thus strain-induced rotations to take place on numerous lattice planes, not only restricted to the grain boundary [54,55]. The dislocation density at the grain interior is comparable to that at the grain boundaries (Fig. 7($b_4$)). The higher dislocation density enhances the strain-hardening rate; the homogeneous distribution of the deformation structure throughout whole grains maintains a highly sustained high strain-hardening rate. Therefore, the combined effects enable the VCoNi alloy to exhibit greater mechanical properties at cryogenic temperatures.

### *4.2. Correlation between the temperature dependence of yield strength and Charpy impact properties*

As presented in Section 3.4, typical single fcc phase HEAs/MEAs such as CrMnFeCoNi and CrCoNi show an increase or maintenance of toughness with decreasing temperature. In addition to the transition of deformation behavior at 77 K, the increase in the area below the strain-stress curves, regarded as toughness, is attributed to the sustained toughness in the aforementioned alloys. However, this explanation does not apply to VCoNi even though both strength and ductility increase at 77 K, because the impact toughness of VCoNi reduces as the temperature decreases.

A property worth considering in VCoNi alloys is the yield strength. The equiatomic VCoNi alloy endures severe lattice distortion and the consequent high friction stress of 383 MPa at 298 K, which is attributed to the considerable fluctuation of the bond distance between V and other elements [5,6]. In addition, according to the interior source model of dislocation generation, the lattice distortion is attributed to both high friction stress and high Hall–Petch coefficient [56]. According to this model, the VCoNi alloy shows a high Hall–Petch coefficient of ~870 MPa $\mu m^{1/2}$, which implies a high sensitivity of stress to grain size. When impact loads are applied to V-notched specimens, the toughness is determined by how much a locally concentrated energy at the notch can be accommodated by plastic deformation. The zone of plastic deformation absorbing the impact energy is called a plastic zone, whose size is related to the yield strength based on the Irwin formula [57]. The yield strength usually increases as temperature decreases, that is, the size of the plastic zone decreases, which affects the Charpy impact energy. Therefore, it is essential to investigate the temperature dependence of the yield strength of VCoNi compared with other HEAs/MEAs to understand the impact energy trend associated with temperature.

According to Wu et al. [58], the temperature dependence of yield strength ($\sigma_{YS}$) is described as

$$\sigma_{YS}(T) = \sigma_a \exp\left(-\frac{T}{C}\right) + \sigma_b \quad (3)$$

where $\sigma_a$, $C$, and $\sigma_b$ are fitting constants. The first term on the right implies the thermal or temperature-dependent part of the yield strength, and here, $\sigma_a$ relates to a rise in yield strength as the temperature decreases. The second term ($\sigma_b$) on the right represents the temperature-independent or athermal part. The yield strength of D10 at 773 K was measured to be 487.8 MPa (curves are not shown here), and all the fitting constants were obtained as listed in Table 3. The temperature dependence of yield strength is plotted in Fig. 8 along with that of the CrCoFeMnNi and CrCoNi alloys [58]. The VCoNi alloy exhibits a much higher value of $\sigma_a$ than the other two alloys: 614 MPa, 489 MPa, and 423 MPa for VCoNi, CrCoNi, and CrMnFeCoNi, respectively. This result indi-

**Table 3**
Calculated constants describing the thermal and athermal parameters in Eq. (3).

| Alloy | $\sigma_a$ (MPa) | $C$ (K) | $\sigma_b$ (MPa) |
|---|---|---|---|
| VCoNi [5] | 614.3 | 203.7 | 474.1 |
| CrCoNi [5,58] | 489 | 228 | 167 |
| CrMnFeCoNi [5,58] | 423 | 180 | 109 |

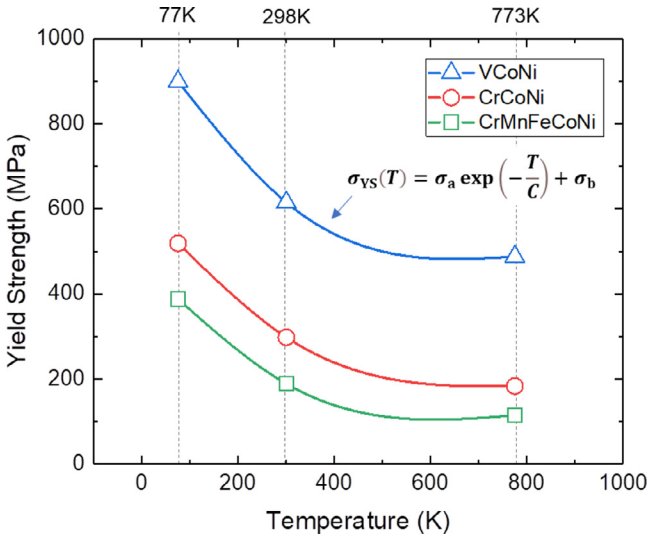


**Fig. 8.** Temperature dependence of the 0.2% offset yield stress of VCoNi, CrCoNi, and CrMnFeCoNi alloys.

cates that VCoNi has the highest temperature dependence of yield strength in these alloys.

The yield strength of pure fcc metals is not very sensitive to the variation in temperature due to the negligible Peierls–Nabarro barriers as has been discussed, e.g., in Ref. [58]. On the other hand, the aforementioned single fcc phase HEAs/MEAs exhibit an increase in yield strength when the temperature is reduced. The yield strength is the sum of the various stresses, of which lattice friction has a temperature-dependent variable. The Peierls–Navarro stress ($\sigma_p$) is the shear stress required to move a dislocation through a crystal lattice in a particular direction, described by [59]:

$$\sigma_p = \frac{2G}{1-\nu}\exp\left(-\frac{2\pi\omega}{b}\right) \quad (4)$$

where $\omega$ is the dislocation width, $G$ is the shear modulus, $\nu$ is Poisson's ratio, and $b$ is the magnitude of the Burgers vector. The dislocation width provides a measure of the degree of disruption that a dislocation creates with respect to the perfect lattice. This term also has a temperature dependence, approximated by Dietze [60]:

$$\frac{\omega}{b} = \left(\frac{\omega}{b}\right)_0 \exp\left(\frac{T}{3T_m}\right) \approx \omega_0\left(1+\frac{T}{3T_m}\right) = \omega_0\left(1+\alpha T\right) \quad (5)$$

where $(\omega/b)_0$ indicates the value at 0 K, $\omega_0$ is the dislocation width at 0 K, $\alpha$ is a small positive constant, and $T_m$ is the melting temperature, ignoring the change in $b$ with temperature and using a simple Taylor expansion. Combining Eqs. (4) and (5), the temperature dependence of the Peierls stress becomes

$$\sigma_p = \frac{2G}{1-\nu}\exp\left(-\frac{2\pi\omega_0}{b}\right)\exp\left(-\frac{2\pi\omega_0}{b}\alpha T\right) \quad (6)$$

In Eq. (6), the most dominant variable of each alloy is $\omega_0/b$ [58,61], since it appears in the exponential expression. Thus, the value of Peierls stress changes according to temperature in an exponential way. In other words, a small dislocation width per unit length of the Burgers vector ($\omega_0/b$) enables the Peierls stress to have a high dependence on temperature. In addition, the reduced dislocation width caused by severe lattice distortion produces high friction stress as dislocation motions become more difficult [61]. This effect is represented by the athermal term $\sigma_b$. Above all, VCoNi has the lowest dislocation width among the considered alloys [58]. It has therefore the largest dependence of temperature on yield strength.

The large temperature dependence of yield strength is directly related to the plastic zone size, as stated above, and consequently to the impact toughness. The stress concentration at the front of the notch and the resulting extent of plastic deformation can be estimated by the Irwin formula:

$$r_p = \frac{1}{6\pi}\left(\frac{K_1}{\sigma_{YS}}\right)^2 \quad (7)$$

where $r_p$ is the plastic zone size, $\sigma_{YS}$ is the yield strength, and $K_1$ is the stress intensity factor. Therefore, the reduction in the plastic zone size would be the largest in the VCoNi alloy according to Fig. 8; hence, the VCoNi alloy cannot absorb the impact energy as much as the CrCoNi or CrMnFeCoNi alloy. Nevertheless, Fig. 5 shows the ductile-dimpled fracture at 77 K, which indicates that a ductile-to-brittle transition does not occur, although the Charpy impact energy decreases with decreasing temperature. Therefore, this study implies that the enhancement of both strength and ductility is not the sole parameter to determine cryogenic damage tolerances for HEAs/MEAs, especially for alloys possessing significant lattice friction stress and temperature dependence. Thus, for the development of high-yield-strength cryogenic alloys, it would be more crucial to alter the deformation mechanism, resulting in vigorous plastic deformation and energy absorption in the plastic zone whose size becomes small at low temperatures.

## 5. Conclusions

In this study, an equiatomic VCoNi alloy was annealed under four different conditions, and its cryogenic tensile and impact properties were evaluated. The cryogenic tensile properties were improved compared to those at room temperature, while the Charpy impact properties gradually decreased with decreasing temperature. The underlying mechanisms determining these properties were investigated in terms of the temperature dependence of yield strength and deformation mechanism, thus resulting in the following conclusions:

(1) The VCoNi alloy exhibited enhanced mechanical properties at 77 K than at 298 K. The well-sustained high hardening rate at 77 K delayed the onset of plastic instability and improved both strength and ductility.
(2) At 298 K, the initiation of a planar glide developed into intertwined dislocation networks of planar dislocation arrays, finally resulting in nano-sized dislocation substructures, called Taylor lattice-like structures. The deformation structures at 77 K were almost identical, indicating that the effect of temperature would be insignificant or different from the existing fcc-structured HEAs/MEAs. The *ab initio* simulations revealed a nearly constant and slightly increasing SFE from 600 K to 0 K for VCoNi, which contributes to much less temperature dependence of deformation structures as compared to the CrCoNi alloy.
(3) Local dislocation substructures were similar at both temperatures, while the dislocation density increased at 77 K, resulting in an enhanced stress and strain-hardening rate according to Taylor's hardening. The highly sustained high strain-hardening rate at 77 K was attributed to the homogeneous distribution of the deformation structure throughout the grains, in contrast to the localization occurring near

grain boundaries at 298 K. Thus, these combined effects enabled the VCoNi alloy to present greater mechanical properties at cryogenic temperatures.

(4) Although a ductile-to-brittle transition was absent, the Charpy impact toughness decreased as temperature decreased, directly relating to the temperature dependence of yield strength. The severe lattice distortion in VCoNi produced a reduced dislocation width and thus, a significant temperature dependence of Peierls stress. The large temperature dependence of yield strength reduced the plastic zone size at the notch tips and consequently restricted the sufficient absorption of impact energies.

## Declaration of Competing Interest

The authors declare that they have no known competing financial interests or personal relationships that could have appeared to influence the work reported in this paper.

## Acknowledgments

This work was financially supported by the National Research Foundation of Korea (NRF-2020R1C1C1003554), the Creative Materials Discovery Program of the National Research Foundation of Korea (NRF) funded by the Ministry of Science and ICT (NRF-2016M3D1A1023384), and the Korea Institute for Advancement of Technology (KIAT) grant funded by the Korea Government (MOTIE, P0002019, The Competency Development Program for Industry Specialist). Fritz Körmann gratefully acknowledges support from the German Research Foundation (Deutsche Forschungsgemeinschaft, DFG) under the priority programme 2006 “CCA–HEA".

## References

[1] X. Chang, M. Zeng, K. Liu, L. Fu, Adv. Mater. 32 (2020) 1907226.
[2] Y. Ye, Q. Wang, J. Lu, C. Liu, Y. Yang, Mater. Today 19 (2016) 349–362.
[3] D.B. Miracle, O.N. Senkov, Acta Mater 122 (2017) 448–511.
[4] Y.A. Alshataif, S. Sivasankaran, F.A. Al-Mufadi, A.S. Alaboodi, H.R. Ammar, Met. Mater. Int. (2019) 1–35.
[5] S.S. Sohn, A. Kwiatkowski da Silva, Y. Ikeda, F. Körmann, W. Lu, W.S. Choi, B. Gault, D. Ponge, J. Neugebauer, D. Raabe, Adv. Mater. 31 (2019) 1807142.
[6] B. Yin, F. Maresca, W. Curtin, Acta Mater 188 (2020) 486–491.
[7] S.S. Sohn, D.G. Kim, Y.H. Jo, A.K. da Silva, W. Lu, A.J. Breen, B. Gault, D. Ponge, Acta Mater (2020).
[8] H. Luo, S.S. Sohn, W. Lu, L. Li, X. Li, C.K. Soundararajan, W. Krieger, Z. Li, D. Raabe, Nat. Commun. 11 (2020) 1–8.
[9] A. Gali, E.P. George, Intermetallics 39 (2013) 74–78.
[10] B. Gludovatz, A. Hohenwarter, D. Catoor, E.H. Chang, E.P. George, R.O. Ritchie, Science 345 (2014) 1153–1158.
[11] G.T. Lee, J.W. Won, K.R. Lim, M. Kang, H.J. Kwon, Y.S. Na, Y.S. Choi, Met. Mater. Int. (2020) 1–10.
[12] G. Laplanche, A. Kostka, C. Reinhart, J. Hunfeld, G. Eggeler, E. George, Acta Mater 128 (2017) 292–303.
[13] M. Yang, L. Zhou, C. Wang, P. Jiang, F. Yuan, E. Ma, X. Wu, Scr. Mater. 172 (2019) 66–71.
[14] D.G. Kim, Y.H. Jo, J. Yang, W.M. Choi, H.S. Kim, B.J. Lee, S.S. Sohn, S. Lee, Scr. Mater. 171 (2019) 67–72.
[15] C. Moussa, M. Bernacki, R. Besnard, N. Bozzolo, IOP Conference Series: Materials Science and Engineering, IOP Publishing, 2015 012038.
[16] H. Gao, Y. Huang, Scr. Mater. 48 (2003) 113–118.
[17] A.J. Wilkinson, D. Randman, Philos. Mag. 90 (2010) 1159–1177.
[18] M. Calcagnotto, D. Ponge, E. Demir, D. Raabe, Mater. Sci. Eng. A 527 (2010) 2738–2746.
[19] P. Denteneer, W. Van Haeringen, J. Phys. C 20 (1987) L883 L887.
[20] A. Zunger, S.H. Wei, L. Ferreira, J.E. Bernard, Phys. Rev. Lett. 65 (1990) 353–356.
[21] G. Kresse, J. Non-Cryst. Solids 192 (1995) 222–229.
[22] G. Kresse, J. Furthmüller, Comput. Mater. Sci. 6 (1996) 15–50.
[23] G. Kresse, D. Joubert, Phys. Rev. B 59 (1999) 1758–1775.
[24] P.E. Blöchl, Phys. Rev. B 50 (1994) 17953–17979.
[25] J.P. Perdew, K. Burke, M. Ernzerhof, Phys. Rev. Lett. 77 (1996) 3865–3868.
[26] M. Methfessel, A. Paxton, Phys. Rev. B 40 (1989) 3616–3621.
[27] D. Ma, B. Grabowski, F. Körmann, J. Neugebauer, D. Raabe, Acta Mater 100 (2015) 90–97.
[28] P. Vinet, J.R. Smith, J. Ferrante, J.H. Rose, Phys. Rev. B 35 (1987) 1945–1953.
[29] A. Otero-de-la-Roza, V. Luaña, Comput. Phys. Commun. 182 (2011) 1708–1720.
[30] V. Moruzzi, J. Janak, K. Schwarz, Phys. Rev. B 37 (1988) 790–799.
[31] S. Sun, Y. Tian, H. Lin, X. Dong, Y. Wang, Z. Zhang, Z. Zhang, Mater. Des. 133 (2017) 122–127.
[32] S. Sun, Y. Tian, H. Lin, H. Yang, X. Dong, Y. Wang, Z. Zhang, Mater. Sci. Eng. A 712 (2018) 603–607.
[33] S.S. Sohn, H. Song, B.C. Suh, J.H. Kwak, B.J. Lee, N.J. Kim, S. Lee, Acta Mater 96 (2015) 301–310.
[34] E. Welsch, D. Ponge, S.H. Haghighat, S. Sandlöbes, P. Choi, M. Herbig, S. Zaefferer, D. Raabe, Acta Mater. 116 (2016) 188–199.
[35] M. Kang, J.W. Won, K.R. Lim, S.H. Park, S.M. Seo, Y.S. Na, Korean J. Met. Mater. 55 (2017) 732–738.
[36] B. Gludovatz, A. Hohenwarter, K.V. Thurston, H. Bei, Z. Wu, E.P. George, R.O. Ritchie, Nat. Commun. 7 (2016) 1–8.
[37] S. Xia, M. Gao, Y. Zhang, Mater. Chem. Phys. 210 (2018) 213–221.
[38] Y.H. Jo, D.G. Kim, M.C. Jo, K.Y. Doh, S.S. Sohn, D. Lee, H.S. Kim, B.J. Lee, S. Lee, J. Alloys Compd. 785 (2019) 1056–1067.
[39] M.J. Jang, H. Kwak, Y.W. Lee, Y. Jeong, J. Choi, Y.H. Jo, W.M. Choi, H.J. Sung, E.Y. Yoon, S. Praveen, Met. Mater. Int. 25 (2019) 277–284.
[40] Y. Kim, H.K. Park, P. Asghari-Rad, J. Jung, J. Moon, H.S. Kim, Met. Mater. Int. (2020) 1–10.
[41] W. Liu, Z. Lu, J. He, J. Luan, Z. Wang, B. Liu, Y. Liu, M. Chen, C. Liu, Acta Mater. 116 (2016) 332–342.
[42] C.C. Tasan, Y. Deng, K.G. Pradeep, M. Yao, H. Springer, D. Raabe, JOM 66 (2014) 1993–2001.
[43] Y. Deng, C.C. Tasan, K.G. Pradeep, H. Springer, A. Kostka, D. Raabe, Acta Mater. 94 (2015) 124–133.
[44] S. Zhao, G.M. Stocks, Y. Zhang, Acta Mater. 134 (2017) 334–345.
[45] J. Ding, Q. Yu, M. Asta, R.O. Ritchie, Proc. Natl. Acad. Sci. U.S.A. 115 (2018) 8919–8924.
[46] H. Huang, X. Li, Z. Dong, W. Li, S. Huang, D. Meng, X. Lai, T. Liu, S. Zhu, L. Vitos, Acta Mater. 149 (2018) 388–396.
[47] C. Niu, C.R. LaRosa, J. Miao, M.J. Mills, M. Ghazisaeidi, Nat. Commun. 9 (2018) 1–9.
[48] X. Zhang, B. Grabowski, F. Körmann, A.V. Ruban, Y. Gong, R.C. Reed, T. Hickel, J. Neugebauer, Phys. Rev. B 98 (2018) 224106.
[49] A. Reyes-Huamantinco, P. Puschnig, C. Ambrosch-Draxl, O.E. Peil, A.V. Ruban, Phys. Rev. B 86 (2012) 060201.
[50] L. Saraf, Microsc. Microanal. 17 (2011) 424–425.
[51] S. Goel, R. Jayaganthan, I. Singh, D. Srivastava, G. Dey, N. Saibaba, Acta Metall. Sin.-Eng. Lett. 28 (2015) 837–846.
[52] B. Gruber, I. Weißensteiner, T. Kremmer, F. Grabner, G. Falkinger, A. Schökel, F. Spieckermann, R. Schäublin, P.J. Uggowitzer, S. Pogatscher, Mater. Sci. Eng. A 795 (2020) 139935.
[53] J.D. Yoo, K.T. Park, Mater. Sci. Eng. A 496 (2008) 417–424.
[54] Z. Xu, H.J. Roven, Z. Jia, Mater. Sci. Eng. A 648 (2015) 350–358.
[55] J. Yoo, S. Hwang, K.T. Park, Metall. Mater. Trans. A 40 (2009) 1520–1523.
[56] R. Armstrong, I. Codd, R.M. Douthwaite, N.J. Petch, Philos. Mag. 7 (1962) 45–58.
[57] D. Broek, The Practical Use of Fracture Mechanics, Springer Science & Business Media, 2012.
[58] Z. Wu, H. Bei, G.M. Pharr, E.P. George, Acta Mater 81 (2014) 428–441.
[59] G.E. Dieter, D.J. Bacon, Mechanical Metallurgy, McGraw-Hill, New York, 1986.
[60] H.D. Dietze, Zeitschrift Fur Physik 132 (1952) 107–110.
[61] Y. Zhao, T. Nieh, Intermetallics 86 (2017) 45–50.